



# A Comparative Tribocorrosion Study of Additive Manufactured and Wrought 316L Stainless Steel in Simulated Body Fluids

Johan Stendal<sup>1</sup> · Omar Fergani<sup>2</sup> · Hitomi Yamaguchi<sup>3</sup> · Nuria Espallargas<sup>1</sup>

Received: 1 July 2017 / Revised: 18 December 2017 / Accepted: 18 December 2017 / Published online: 4 January 2018  
© Springer International Publishing AG, part of Springer Nature 2018

## Abstract

In this study, the corrosion and tribocorrosion behavior of additive manufactured (AM) 316L is investigated and compared to wrought 316L. The experiments were performed in both a 0.9 wt% NaCl solution and a simulated body fluid based on the protein albumin. The results are interpreted based on the analysis of the microstructure, inherent AM porosities and surface roughness. The results confirm that the AM samples present a substandard behavior compared to the wrought materials due to the higher surface area caused by the voids inherent to the AM process.

**Keywords** Bio-tribocorrosion · Additive manufacturing · 316L

## 1 Introduction

Stainless steels are well known for their good corrosion resistance due to the formation of a homogeneous and uniform oxide layer (i.e., passive film) of mainly Cr<sub>2</sub>O<sub>3</sub> [1, 2]. However, the corrosion resistance of stainless steels can vary depending on the grade used. The AISI 316L grade has been widely used in biomedical implants due to its low carbon content and biocompatibility and has displayed very good performance [3]. Traditionally, these implants are manufactured using casting processes, and recently, 3D-printing or additive manufacturing is emerging as a promising process for the orthopedic implant industry.

Additive manufacturing (AM) promises to revolutionize the field of orthopedic medical implants. AM is enabling the development of patient-specific implants which offer better mobility, mechanical properties and lifetime [4]. In addition, AM technology allows the possibility to manufacture an implant surface which supports osseointegration, which is direct bone-to-implant contact without intervening

connective tissue. Osseointegration induces osteogenesis (i.e., bone healing) [5, 6]. Selective laser melting (SLM) is seen as one of the most promising AM processes. During SLM, layers of fine atomized metal powder are evenly distributed on a substrate plate, taking place in a controlled atmosphere of inert gas. A laser selectively melts the powder according to given coordinates, fusing each slice of the geometry. Once a layer is finished, a new layer of powder is distributed on top and the process repeats. After the last step, the metal object can be retrieved from the powder, with a geometry closely matching the computer drawing. The utilization of 316L in additive manufacturing, and specifically powder bed-based processes, is growing significantly due to the high weldability of this material. Recently, several studies have reported on the applications of 316L as additive manufactured biomedical implants [7, 8].

In spite of the recent advances done in additive manufacturing, producing fully dense parts without porosities is still a challenge. Traditionally, the surface roughness obtained using AM is poor compared to wrought finishing processes. Thus, surface post-processing of AM components is needed. For example, the surface finish can be enhanced using a remelting strategy during selective laser melting [9]. This is particularly the case for applications where the surface is required to have a specific roughness, such as knee implants. In a recent work of [10], magnetic abrasive polishing and burnishing are used on selective laser melted 316L to enhance both the surface roughness and the surface properties by inducing compressive residual stresses. Indeed,

✉ Omar Fergani  
omar.fergani@siemens.com

<sup>1</sup> Department of Mechanical and Industrial Engineering, NTNU, Richard Birkelands vei 2B, 7491 Trondheim, Norway

<sup>2</sup> Siemens Software Industry, Leuven, Belgium

<sup>3</sup> Department of Mechanical and Aerospace Engineering, University of Florida, Gainesville, FL, USA

Bercot et al. [11] demonstrated that compressive residual stress can enhance corrosion resistance.

When a surface is exposed to a corrosive environment, a passive oxide film spontaneously forms on the surface of a metallic material in the presence of oxygen [2]. If a passive metal suffers mechanical damage (i.e., sliding under contact force), the passive film is destroyed (depassivation). However, when the mechanical action ceases, the passive film rapidly restores (repassivation). If this process occurs when a passive metal is exposed to a corrosive electrolyte, the corrosion rate will increase due to exposing the bare metal surface to the corrosive environment, leading to a phenomenon known as wear-accelerated corrosion. This process is known as tribocorrosion [12–14].

For evaluating the tribocorrosion performance of passive metals, potentiostatic and open-circuit potential (OCP) measurement methods are most frequently used, owing to their simplicity and ability to quantify wear and corrosion rates. In addition, models for tribocorrosion are available in the literature allowing prediction of wear and corrosion rates [12, 15–18]. Stainless steels have been extensively subjected to tribocorrosion studies in the last decades [3, 5, 11, 19–21]. These studies have shown that the passive nature of stainless steels is detrimental for wear and corrosion rates under tribocorrosion conditions. Typically, an increase in electrode potential during rubbing leads to an increase in wear rates and passive dissolution. To minimize this effect, several researchers have investigated the possibility of using surface modifications of passive metals, such as plasma nitriding [22–27]. The tribocorrosion behavior of AISI 310 and AISI 316 stainless steels has been studied under reciprocating sliding conditions in 3.5% NaCl, using a pin-on-disk tribometer integrated with a potentiostat for electrochemical control [3, 11, 20, 21, 28–30]. Other researchers have used a similar approach to characterize the tribocorrosion behavior of different biomaterials such as CoCr alloys [4, 22]. In other studies, the impact of chemical composition was investigated, aiming to enhance corrosion resistance [28–30].

To the best knowledge of the authors, no previous investigation of the tribocorrosion of AM 316L is found in the literature. This study is presented in the format of a comparative study and aims to provide the basis of understanding the tribocorrosion behavior of additive manufactured components.

The aim of this study is to compare the tribocorrosion behavior of wrought and AM 316L stainless steel alloy. In the first section, an overview of the state of the art is presented. Then, a detailed description of the experimental work is provided for both the tribocorrosion test and the materials characterization. The obtained results were presented and analyzed to build a basis for the conclusion section. The final section provides the conclusions of the tribocorrosion behavior of AM 316L stainless steel.

## 2 Experimental Procedure

### 2.1 Materials

The wrought test samples were cast and subsequently rolled 316L stainless steel. The additive test samples were 316L stainless steel manufactured by using selective laser melting (SLM) in a Concept Laser M2-200W. Standard 316L parameters were applied to the diode pumped Yb-fiber laser. The used process parameters are: power of 180 W; laser speed of 800 mm/s; hatch spacing of 0.105 mm; and layer thickness of 0.03 mm. The wrought samples were hot-rolled at 700 C and then annealed at 1100 C for 10 min, followed by air cooling before finally machining the surface using standard milling conditions. All samples were cylindrical with 5 mm thickness and 25 mm diameter. Both the additive manufactured and wrought samples were polished to mirror finish using the same procedure and setup to achieve similar final surface roughness. The test face was grinded gradually to a 10  $\mu\text{m}$  surface roughness, before being polished down to the final mirror surface finish of 1  $\mu\text{m}$  using diamond particles. Before each experiment, the samples were cleaned with acetone in an ultrasonic bath for 5 min, followed by cleaning with distilled water in an ultrasonic bath for 5 min before rinsing in ethanol and final drying.

### 2.2 Tribocorrosion Tests

Two different solutions were used to investigate the tribocorrosion behavior of the 316L stainless steel samples. The first solution was an aqueous solution with 0.9 wt% sodium chloride (NaCl) in distilled water, the same concentration found in the human body. The second solution was a simulated body fluid (SBF) consisting of distilled water, 0.9 wt% sodium chloride (NaCl), 0.74 wt% dipotassium monohydrogen phosphate ( $\text{K}_2\text{HPO}_4$ ), 0.1 wt% potassium dihydrogen phosphate ( $\text{KH}_2\text{PO}_4$ ) and 0.05 wt% of the bovine serum albumin (BSA) protein in crystallized form.

The experimental setup is shown in Fig. 1. The setup consists of a three-electrode tribo-electrochemical cell with a reciprocating ball acting as a counterpart sliding on the flat surface of the stainless steel material. The electrochemical cell consists of a platinum counter electrode, an Ag/AgCl (3M KCl) reference electrode and the 316L sample as the working electrode. All potentials reported in this paper will be relative to the Ag/AgCl (3M KCl) reference electrode, which has a difference of 0.225 V with the standard hydrogen electrode. The electrolytes during tribocorrosion testing were kept at 37 °C with a heated tube as shown in Fig. 1.

The reciprocating ball was 6 mm in diameter and made of the bioinert material alumina ( $\text{Al}_2\text{O}_3$ ). A normal load

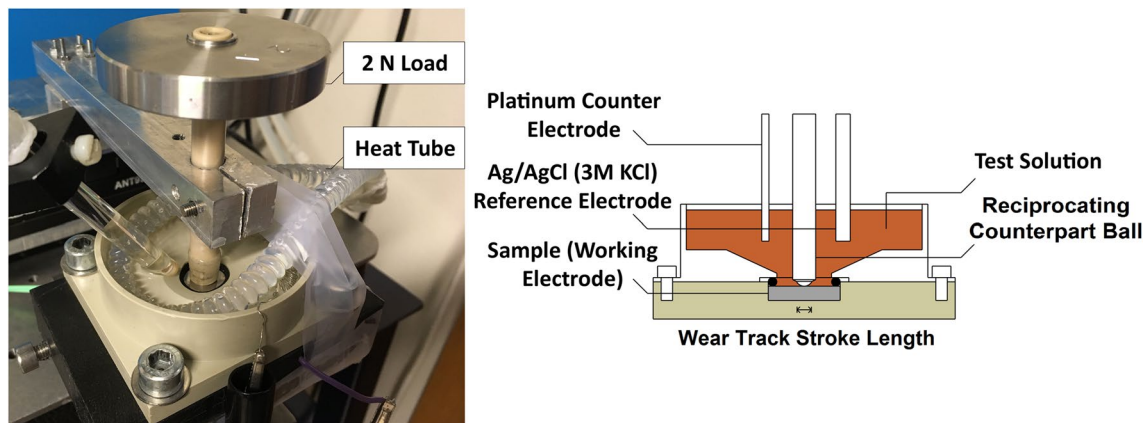


**Fig. 1** Tribocorrosion setup

of 2 N was used and applied as dead weight. The sliding frequency was set to 1 Hz, and the stroke length was 5 mm. An initial stabilization period of 10 min was first recorded, and then the tribometer was run for 3600 cycles (i.e., 1 h) before a final stabilization period of 10 min was recorded. In potentiodynamic tests performed in both the NaCl and the SBF solutions, the 316L samples were passive at around  $-200$  mV; therefore, this potential value was used in all the anodic potentiostatic tribocorrosion experiments.

At least two repetitions of each test have been performed for evaluating the repeatability of the tests. Since no major differences were found, only one repetition will be plotted in the upcoming sections of the paper for clarity. When data are reported in tables, all the results are provided.

### 3 Results and Discussion

#### 3.1 Microstructural Analysis

To better understand and assess the deformation of the samples during the rubbing process, the microstructure and mechanical properties were investigated using electron backscatter microscope (EBSD) and scanning electron microscope (SEM). The hardness measurements on the mirror-polished samples for the additive manufactured (AM) and wrought 316L samples were 220 and 152 HV, respectively. Figure 2 shows the SEM and EBSD pictures of the powder and the AM sample together with an EBSD image of the wrought sample as comparison. The average grain size of the AM samples was around 10 microns, as shown in (c), with a dendritic subgrain structure varying between 0.5 and 1 micron, as shown in (e). For comparison, the wrought material has an average grain size of about 20 microns, as shown in (f). The additive manufactured sample

shows also elongated grains following the build direction. It is noteworthy that the AM samples also had a strong texture in the (001) direction, as shown in (d). The optical micrograph image in (c) shows that the AM samples presented some pores compared to the fully dense wrought sample. The wrought materials demonstrated elongated grains in the rolling direction, as shown in (f).

#### 3.2 Electrochemical Analysis

The electrochemical experiments were performed in both 0.9 wt% NaCl and the simulated body fluid with albumin for the wrought and AM samples. In total, each experiment was repeated six times to achieve consistent results. Very consistent results were obtained, and thus, only one curve per sample is plotted in Figs. 3 and 4.

Figure 3 shows the polarization curves of wrought and additive 316L in a 0.9 wt% NaCl solution. Wrought and additive 316L showed passive potential intervals of 317 mV and 569 mV, respectively. Taking the 41 mV difference in rest potentials into account, the difference in passive interval lengths was 211 mV ( $\Delta E$ ). This suggests that additive 316L requires more electric potential energy before the breakdown potential is reached, than that of wrought 316L in a 0.9 wt% NaCl solution. Noise in the polarization curves during the range of the passive potential can be observed in all the results with the NaCl solution, with more prominent noise and higher peaks in the results of wrought 316L. These peaks indicate the occurrence of metastable pitting, suggesting that wrought 316L undergoes metastable pit growth during its passive potential interval. These findings were confirmed in optical microscope observations. The curve of wrought 316L shows continuous metastable pitting from around  $-33$  mV to the breakdown potential, where stable pit growth was initiated. The curve of additive 316L shows an almost constant corrosion current during the

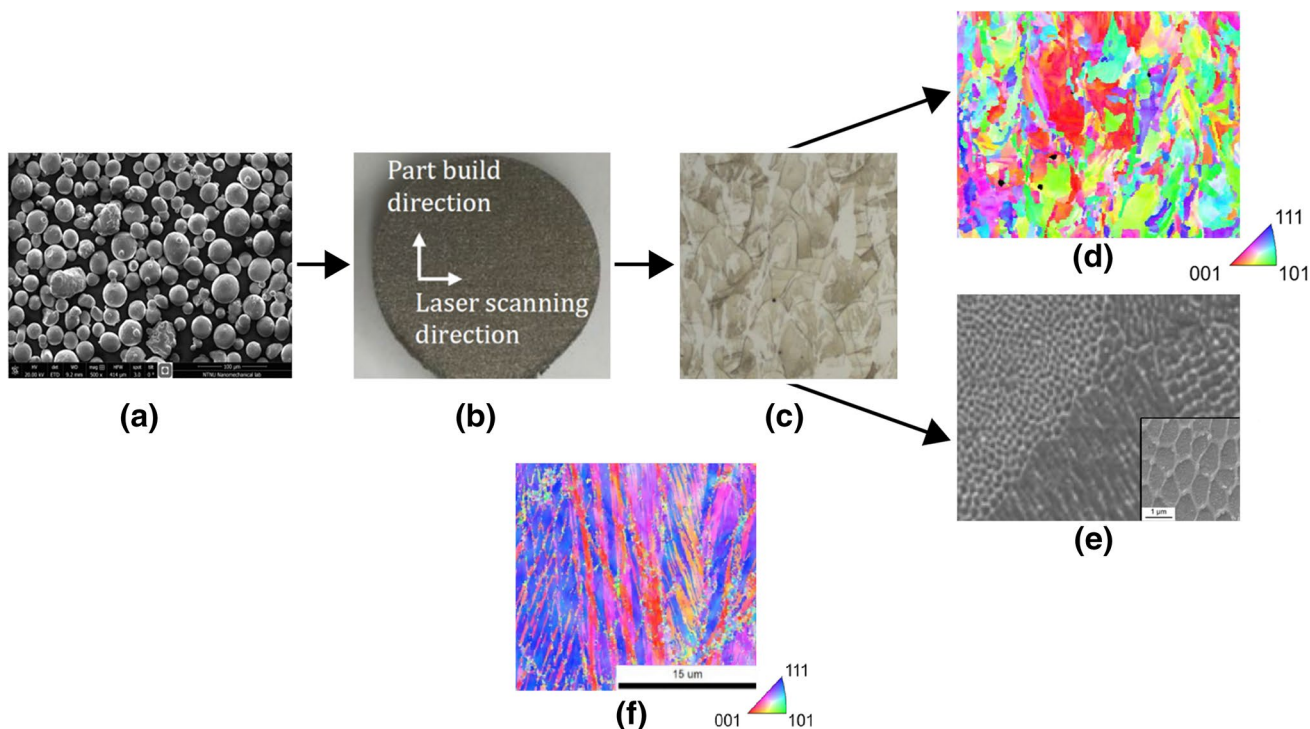


**Fig. 2** **a** 316L powder used to produce the samples; **b** the as-built samples; **c** optical micrograph showing the melt pools; **d** EBSD scan showing elongated grain in the build direction; **e** SEM image showing dendritic phase; **f** EBSD of wrought sample

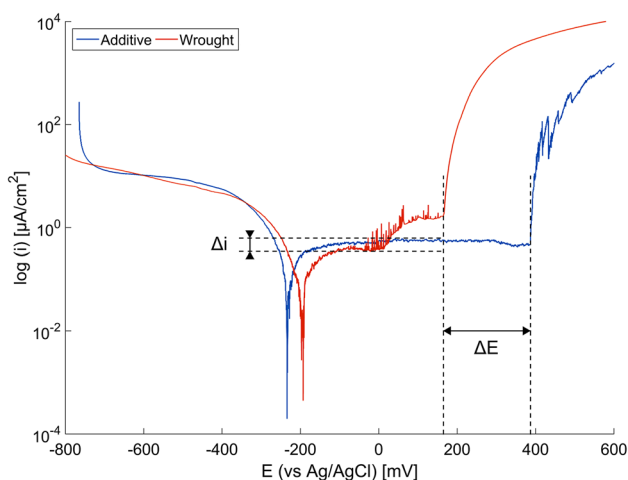


**Fig. 3** Polarization curves of wrought and AM 316L in 0.9 wt% NaCl

passive interval, indicating there was little to no metastable pit growth before the breakdown potential was reached. This suggests that wrought 316L is more susceptible to metastable pit growth than additive 316L in a 0.9 wt% NaCl solution.

The 211 mV ( $\Delta E$ ) longer passivation range in the AM sample can be due to many factors, such as grain size, surface chemistry (i.e., main alloying elements and their distribution), temperature, electrolyte composition [2]. In this

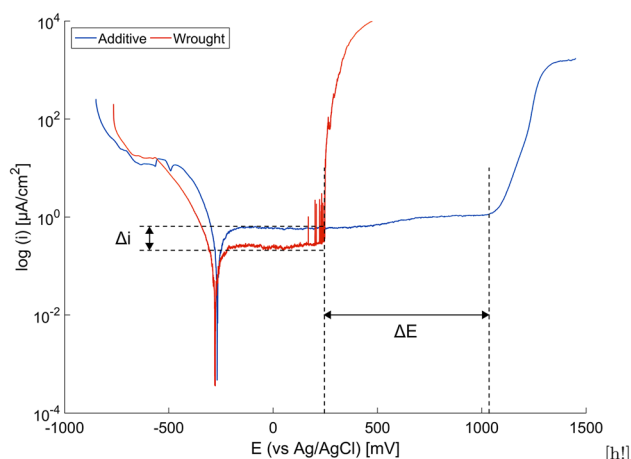


**Fig. 4** Polarization curves of wrought and AM in simulated body fluid

particular case, the breakdown potential for the AM sample was reached at around 400 mV (vs. the Ag/AgCl reference electrode), which corresponds to the dissolution of Cr ions [31]. In the case of the wrought sample, the breakdown potential happens earlier due to the metastable pitting of the passive film. In both the AM and the wrought samples, the cathodic behavior was very similar, although hydrogen evolution started earlier in the AM sample (at around  $-750$  mV).

Figure 4 shows the polarization curves of wrought and additive 316L in a simulated body fluid. Wrought and additive 316L showed passive potential intervals of 459 and 1205 mV, respectively, in a simulated body fluid. Taking the slight difference in rest potentials of around 12 mV into account, the difference in passive interval lengths was 734 mV ( $\Delta E$ ). This suggests that the AM samples require more electric potential energy before the breakdown potential is reached, than that of the wrought material version in a simulated body fluid.

Interestingly, in the presence of the albumin proteins, the breakdown potential for the AM sample corresponds to the potential for water oxidation, which suggests that the passive film was indeed unaffected [31]. This may be due to the albumin proteins acting as a barrier for oxidants increasing the capacity of the material to withstand electric potential before the dissolution of any of the alloying elements happen [4]. In the case of the wrought sample, the breakdown potential was also delayed (up to ca. 250 mV) suggesting some improvement in the presence of proteins. However, it is not enough to prevent pitting. As expected, proteins have a strong effect in the cathodic kinetics enhancing them [32]. As seen in the cathodic branch, the hydrogen evolution occurs already at around  $-400$  mV. In addition, there was an increase in passive dissolution of the AM sample with respect to the wrought sample. This effect is clearly seen in the higher current density for the AM sample (see  $\Delta i$  in Fig. 4).

### 3.3 Tribocorrosion at Open-Circuit Potential

At the open-circuit potential (OCP), the anodic and cathodic reaction rates of the metal alloy exposed to the electrolyte are equal, providing a net corrosion current of zero. These equilibrium conditions are disturbed when mechanical action is applied in an electrochemical system at the OCP. Hence, the OCP test in tribocorrosion can be used to identify whether the material is active or passive in a given environment [12]. This phenomenon is well illustrated in Fig. 5 where the potential immediately drops at the onset of rubbing and recovers when rubbing finishes. This is known as depassivation, and it is characterized by a cathodic potential drop. This depassivation process leads to the formation of a galvanic couple leading to the release of electrons from the worn area resulting in a corrosion and wear rates increase.

Figure 5 shows the potential evolution with time for the OCP measurements of the wrought and AM 316L in a 0.9 wt% NaCl solution. The data show an open-circuit potential of around  $-71$  and  $-157$  mV for wrought and AM 316L, respectively, before rubbing conditions were applied. When rubbing starts, the wrought samples show an initial potential drop to around  $-289$  mV, and continued to oscillate around this value throughout the experiment. The AM samples show

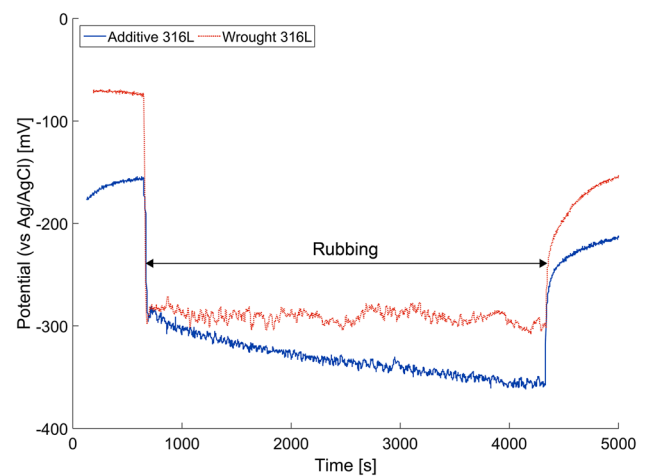


Fig. 5 OCP curves for wrought and AM 316L in 0.9 wt% NaCl

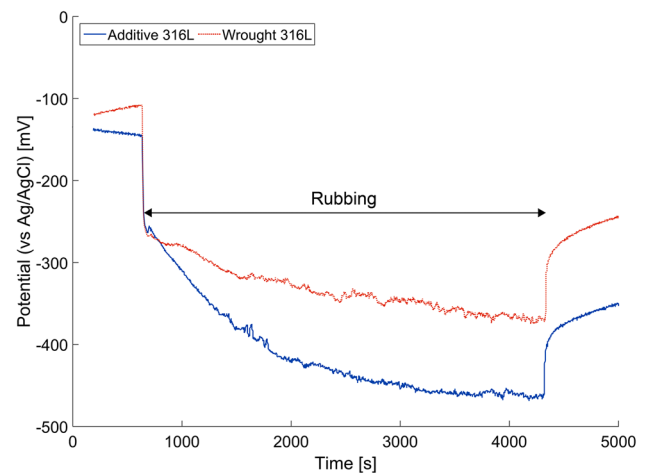


Fig. 6 OCP curves for wrought and AM 316L in SBF

an initial potential drop to around  $-295$  mV, but keeps a continuous decay during rubbing to around  $-355$  mV. Once the rubbing stops the potential gradually recovered in all samples. The AM samples show a decrease in potential during rubbing conditions by around 60 mV, while the wrought samples show a near constant OCP during rubbing.

Figure 6 shows the potential plotted against time for the OCP measurements of the wrought and AM manufactured 316L in SBF. Interestingly, the drop in the potential in this condition was similar for both samples at the onset of rubbing and kept a continuous decay during rubbing. However, this decay was more pronounced for the AM sample. The OCP before rubbing was around  $-109$  and  $-142$  mV for wrought and AM 316L, respectively. The wrought samples show an initial potential drop to around  $-267$  mV, decreasing to around  $-368$  mV. For comparison, the additive samples show an initial potential drop to around  $-263$  mV,

decreasing to around  $-460$  mV. When rubbing stops, the repassivation process happens gradually and at a lower speed than in the case of the tests in NaCl.

The wrought samples display a nearly constant OCP during rubbing conditions in NaCl, as observed in Fig. 5. This indicates that the material is able to uphold a near steady state equilibrium between the mechanical depassivation and electrochemical repassivation surface processes. The AM samples show higher and faster potential drops in both solutions (Figs. 5, 6), indicating that the electrochemical repassivation is not able to keep up with the mechanical depassivation process. This demonstrates that the AM samples possess inferior tribocorrosion performance, as compared to the wrought samples. The underlying mechanics causing this difference in potential drops is still unknown to the authors, and will need to be investigated in more detail in future work.

As mentioned in the previous section, the proteins led to an increase in the cathodic kinetics of the metals. Therefore, it is not surprising to observe a much bigger cathodic potential decay during rubbing of the AM and wrought samples in the presence of albumin. This was due to the higher cathodic current generated as a consequence of the higher cathodic activity (i.e., hydrogen evolution). Indeed, higher cathodic currents were measured during the polarization curves and hydrogen evolution was found to happen already at  $-400$  mV. Interestingly, the potential drop of the AM sample reaches that value and therefore one can expect breaking of disulfide bonds of the protein by the hydrogen action [33]. This was demonstrated later with the lower material loss found on the samples tested in albumin at OCP with respect to the ones tested in NaCl. Interestingly, the initial cathodic potential decay of the AM sample was the same in both electrolytes and still big differences in material loss were found (i.e., almost double material loss in NaCl, as shown in Fig. 5). Therefore, the cathodic drop in SBF can be mostly related to the enhanced cathodic kinetics, due to the presence of the albumin proteins.

### 3.4 Potentiostatic Tribocorrosion

In the potentiostatic tests, a potential was applied to the working electrode to investigate the evolution of the corrosion current. If the tests are performed at the passive potential of the sample in the electrolyte, the mechanical depassivation and electrochemical repassivation under tribocorrosion conditions occur. The AM and wrought samples were both passive at around  $-200$  mV in both the NaCl and the SBF solutions. Figure 7 shows the coefficient of friction (COF) and current evolution with time for the passive potentiostatic tests in 0.9 wt% NaCl. The passive layer is damaged at the onset of rubbing and the corrosion current

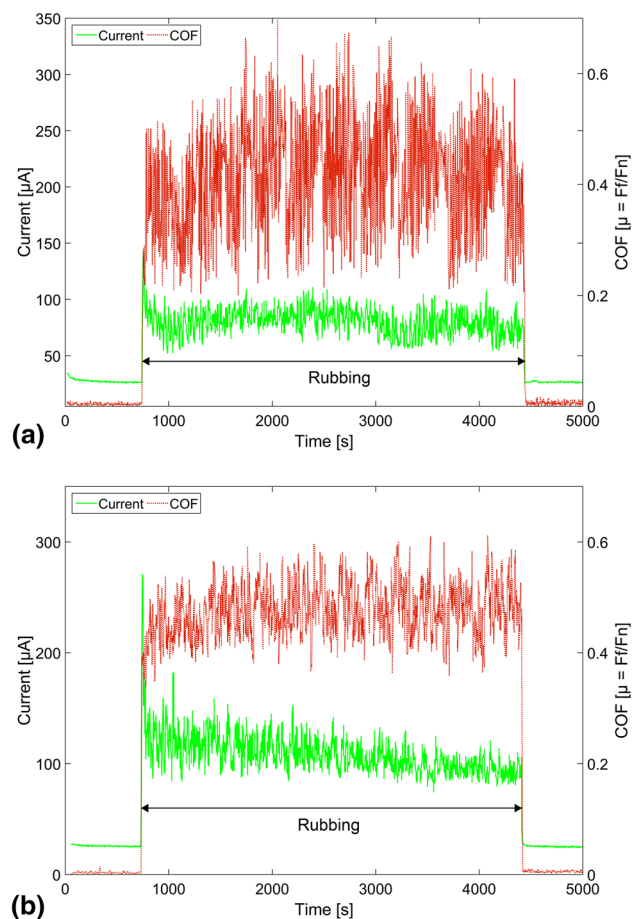


**Fig. 7** **a** Potentiostatic test on wrought in 0.9 wt% NaCl; **b** potentiostatic test on AM 316L in 0.9 wt% NaCl

increases, indicating the increase in the corrosion rate due to the wear-accelerated corrosion mechanism [12].

Figure 7 shows the coefficient of friction and current plotted against time for the potentiostatic measurements of wrought and AM 316L in a 0.9 wt% NaCl solution. The data show a current before rubbing oscillating around  $26 \mu\text{A}$  for wrought 316L and around  $25 \mu\text{A}$  for AM 316L under this condition. During rubbing, the wrought samples show an average COF value oscillating around 0.4, while the AM samples show an average COF value oscillating around 0.5. The rubbing current reaches an initial high point of around  $142 \mu\text{A}$  for the wrought steel and  $270 \mu\text{A}$  for the AM manufactured steel before gradually decreasing, and oscillating around an average value of  $86 \mu\text{A}$  for wrought steel and  $110 \mu\text{A}$  for AM steel. As the rubbing ceases, the corrosion current drops to oscillate around its original value of around  $26 \mu\text{A}$  for wrought and  $25 \mu\text{A}$  for the AM samples.

Figure 8 shows the coefficient of friction and current plotted against time for the potentiostatic measurements of wrought and AM 316L in a simulated body fluid with protein albumin. The data show a current before rubbing

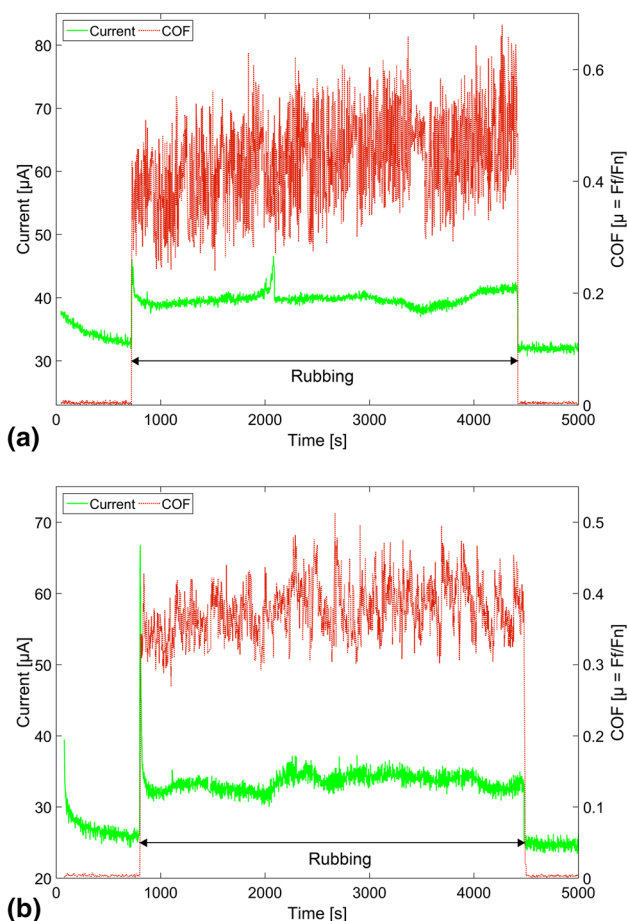


**Fig. 8** **a** Potentiostatic test on wrought in SBF; **b** potentiostatic test on AM 316L in SBF

oscillating around 33 µA for wrought 316L and at 26 µA for AM 316L. During rubbing, the wrought samples show an average initial COF value oscillating around 0.4 which gradually increases, stabilizing at 0.5. The AM samples show a COF value oscillating around 0.4. During rubbing, the current reaches an initial high point of around 46 µA for wrought samples and 67 µA for AM samples, before decreasing and oscillating around an average value of 40 µA for wrought and 34 µA for additive manufactured samples. As the rubbing conditions ceases, the corrosion current drops to oscillate around its original value of around 33 µA for the wrought samples and 26 µA for the AM samples.

**Table 1** Difference between the rest corrosion current during static conditions and the average corrosion current during rubbing ( $\Delta I$ )

Electrolyte	Sample	$\Delta I$ Test 1 ( $\mu A$ )	$\Delta I$ Test 2 ( $\mu A$ )	$\Delta I$ Test 3 ( $\mu A$ )	Std. deviation
0.9 wt% NaCl	Wrought	60	59	64	2.2
	Additive	85	81	84	1.7
SBF	Wrought	7	7	7	0.0
	Additive	8	9	8	0.5

Table 1 shows the difference in corrosion current  $\Delta I$  from all the potentiostatic tests in both electrolytes.  $\Delta I$  is the difference between the corrosion current before rubbing and the average corrosion current during rubbing. Although wrought 316L shows a higher absolute corrosion current than AM 316L in the SBF, the difference in corrosion current of wrought 316L was lower than additive 316L in all tests. This suggests that wrought 316L undergo a lower increase in corrosion rate from static to rubbing conditions than additive 316L in both electrolytes. This is indeed expected since more passive dissolution of the additive manufactured sample was already observed in the polarization curves in both electrolytes (Fig. 4).

The difference in corrosion currents of wrought and additive 316L decreased on average by around 88 and 90%, respectively, in the simulated body fluid, as compared to the NaCl solution. This suggests that both the wrought and additive samples undergo decreased corrosion rates in the simulated body fluid. This may be due to the albumin proteins blocking oxidants from accessing the material surface, inhibiting the corrosion rate [32].

### 3.5 Material Loss and Wear Tracks

Figures 9 and 10 show optical images taken of the samples with the Alincola white-light interferometer after testing in 0.9% NaCl and SBF, respectively. They show the wear tracks formed after the tribocorrosion experiment was concluded, with the scale given in the bottom right corner. The wear track width and depth as illustrated in Fig. 11 were measured with the Alicona software, and the results are summarized in Table 2. By approximating the wear track shape to a cuboid, its volume can be calculated by multiplying the height, width and length (a constant 5 mm stroke length). The calculated wear track volume gives an indication of the volumetric material loss caused by the tribocorrosion test.

Figures 12 and 13 provide a summary of the calculated volumetric material losses from all the OCP and potentiostatic tests, respectively. The results show around the same average volume loss for the OCP and potentiostatic tests, for both material versions and both electrolytes. In all testing conditions, the presence of albumin led to a lower material loss. In general, the material loss differences between wrought and AM samples were minimal in both electrolytes despite the clear differences in

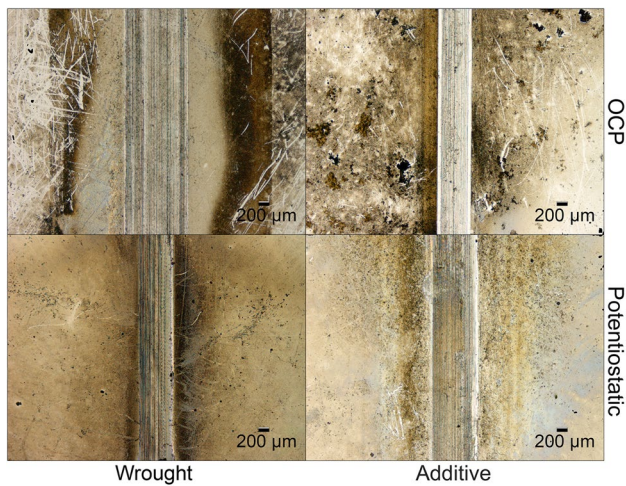


**Fig. 9** Wear tracks in 0.9 wt% NaCl

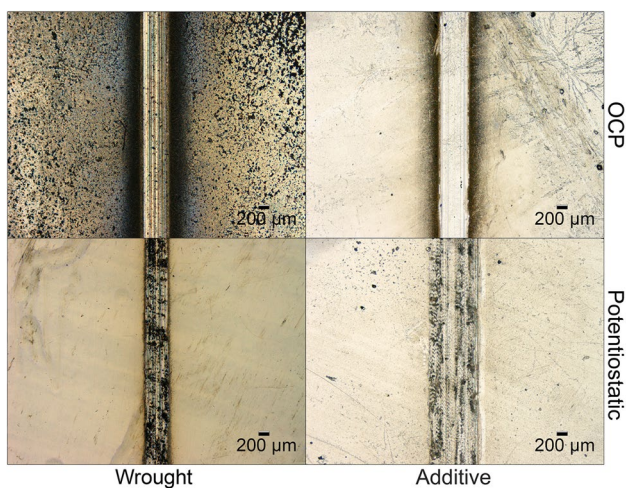


**Fig. 10** Wear tracks in SBF

electrochemical behavior. Interestingly, the larger potential drop found when testing in albumin did not lead to higher material loss indicating that there was very little wear-accelerated corrosion. Indeed, Fig. 13 clearly shows less material loss. This indicates that the increased cathodic

kinetics in protein with the early formation of hydrogen are in fact used to break the disulfide groups of the protein increasing the adhesion to the metallic surface and thus hindering the mechanical damage.

The results of the potentiostatic tests are more controversial, since one would in fact expect more material loss of the AM samples, as both the electrochemical and the tribocorrosion tests showed a clear increase in corrosion current leading to an increase in passive dissolution. The lower current measured in the presence of albumin indeed resulted in less material loss in this electrolyte. It is very difficult to speculate whether the higher hardness of the AM sample could be the responsible for this unexpected behavior, or whether subsurface effects or even subsurface accumulated stresses could be the cause. In addition, no chemical study of the passive films was performed in this work. Therefore, this needs more research and will not be discussed further.

Overall, the compilation of data from both the electrochemical analysis and the potentiostatic experiments suggests that the AM samples demonstrate inferior tribocorrosion performance, especially when looking at the enhancement in passive dissolution rates. However, the AM samples display better performance regarding material loss. Several paths were explored in this study to interpret these results starting from the influence of the microstructure that appears very small and cannot explain the obtained results. The influence of the surface roughness alone was explored and demonstrated that both the AM and wrought samples showed the same surface roughness. Finally, an in-depth analysis of the corrosion mechanisms and specifically the increased surface area in the case of AM 316L, due to the inherent defect in the AM process, can explain the inferior tribocorrosion performance in SBF. Despite the results obtained in this study, other hypothesis related to the interaction of the protein with the AM metal shall be explored in future work to better understand this mechanism. Also, the subsurface deformations and tribofilms formed in the AM samples should be evaluated in a continuation work to further understand the mechanisms.

**Table 2** Measurements of the wear track width (w) and depth (d) for all the tested conditions

Electrolyte	Sample	Type	Test 1 (w/d) (μm)	Test 2 (w/d) (μm)	Test 3 (w/d) (μm)
0.9 wt% NaCl	Wrought	OCP	367/7.7	459/5.1	422/5.9
		Pot	557/4.9	299/6.8	552/4.5
	Additive	OCP	320/7.1	384/6.3	345/5.9
		Pot	366/5.2	323/7.4	400/5.6
SBF	Wrought	OCP	402/3.3	410/2.7	293/3.9
		Pot	517/2.2	239/3.4	236/5.1
	Additive	OCP	250/3.1	320/3.5	390/2.5
		Pot	269/3.9	468/1.8	289/3.5



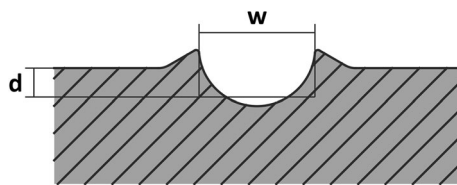


**Fig. 11** Wear track illustration

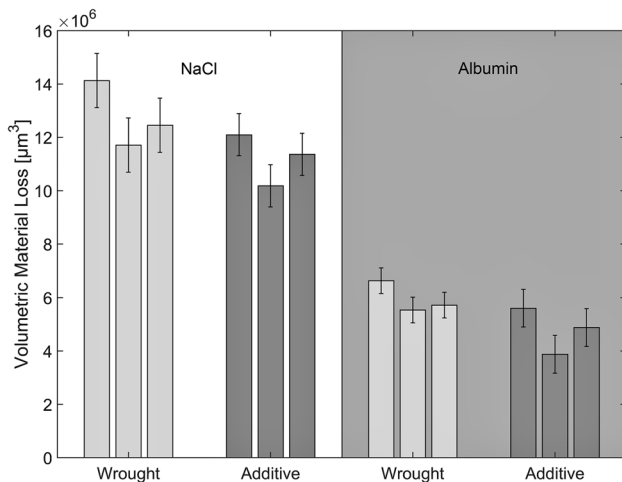


**Fig. 12** Average volumetric material loss from OCP tests

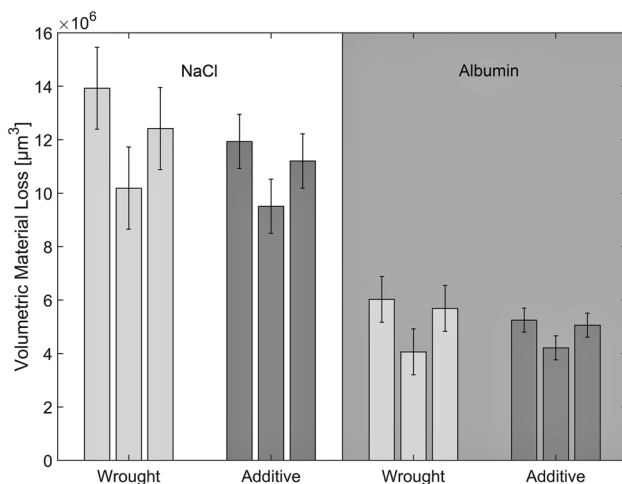


**Fig. 13** Average volumetric material loss from potentiostatic tests

## 4 Conclusions

In this study, the bio-tribocorrosion behavior of additive manufactured 316L stainless steel is compared to its wrought counterpart. The experiments were performed in both a 0.9 wt% NaCl solution and a simulated body fluid (SBF). In the electrochemical analysis the mechanics of

metastable pitting and dissolution of Cr ions are important topics of discussion, as well as the effects of the albumin proteins. In the tribocorrosion tests, the open-circuit potential, corrosion current, coefficient of friction and wear loss were measured. The protein interactions, electrochemical kinetics, surface chemistry and microstructure are important topics of discussion here. The main conclusions drawn from this investigation are as follows:

- The electrochemical analysis revealed a higher passivation capacity for the AM samples as compared to the wrought samples. In addition, the AM samples displayed less susceptibility to metastable pitting.
- The AM samples displayed higher OCP drops during rubbing conditions in both solutions compared to the wrought samples, indicating that the wrought samples are better able to uphold a steady state equilibrium between the mechanical depassivation and electrochemical repassivation processes.
- The potentiostatic experiments revealed that the wrought samples undergo a lower increase in corrosion current (i.e., corrosion rate) during rubbing conditions, as compared to the AM samples.
- The AM samples displayed less material loss in the tribocorrosion experiments in both solutions.

The electrochemical and tribocorrosion results of the AM samples indicate enhanced corrosion kinetics when compared to the wrought samples. This does not correlate with the wear results found, which were better than expected. The differences in microstructure and surface roughness were too small to account for the different results for the two material versions. This points to the mechanical behavior and the inherent porosities of the AM samples playing major role in the corrosion and tribocorrosion performance of the material and shall be studied further.

**Acknowledgements** The authors would like to thank Cristian Torres for his help in conducting the experiments and Vegard Brtan for his help with the SLM process. The authors would like to acknowledge the support from the research center 'SFI Manufacturing' and the MKRAM project (Grant No. 248243), which is sponsored by the Research Council of Norway and industrial partners.

## Compliance with ethical standards

**Conflict of interest** On behalf of all authors, the corresponding author states that there is no conflict of interest.

## References

1. Olsson COA, Landolt D (2001) Film growth during anodic polarization in the passive region on 304 stainless steel with Cr, Mo and

- W additions studied with EQCM and XPS. *J Electrochem Soc* 148:B438–B449
2. Olsson COA, Landolt D (2003) Passive films on stainless steels—chemistry, structure and growth. *Electrochim Acta* 48:1093–1104
  3. Jemmely P, Mischler S, Landolt D (1999) Tribocorrosion behaviour of Fe–17Cr stainless steel in acid and alkaline solutions. *Tribol Int* 32:295–303
  4. Wang Z et al (2016) Effect of proteins on the surface microstructure evolution of a CoCrMo alloy in bio-tribocorrosion processes. *Colloids Surf B Biointerfaces* 145:176–184
  5. Bidiville A et al (2007) Effect of surface chemistry on the mechanical response of metals in sliding tribocorrosion systems. *Wear* 263:207–217
  6. Albrektsson T, Johansson C (2001) Osteoinduction, osteoconduction and osseointegration. *Eur Spine J* 10:96–101
  7. Sin JR (2015) Investigation of the corrosion and tribocorrosion behaviour of metallic biomaterials. Doctoral Thesis, Luleaa University of Technology
  8. Yan Y (2006) Corrosion and tribocorrosion behaviour of metallic orthopaedic implant materials. Doctoral Thesis, The University of Leeds
  9. Vaithilingam J et al (2016) The effect of laser remelting on the surface chemistry of Ti6Al4V components fabricated by selective laser melting. *J Mater Process Technol* 232:1–8
  10. Yamaguchi H, Fergani O, Pei-Ying W (2017) Modification using magnetic field-assisted finishing of the surface roughness and residual stress of additively manufactured components. *CIRP Ann Manuf Technol* 66:305–308
  11. Henry P, Takadoum J, Bercot P (2009) Tribocorrosion of 316L stainless steel and TA6V4 alloy in H<sub>2</sub>SO<sub>4</sub> media. *Corros Sci* 51:1308–1314
  12. Mischler S (2008) Triboelectrochemical techniques and interpretation methods in tribocorrosion: a comparative evaluation. *Tribol Int* 41:573–583
  13. Mischler S, Debaud S, Landolt D (1998) Wear accelerated corrosion of passive metals in tribocorrosion systems. *J Electrochem Soc* 145:750–758
  14. Munoz AI, Espallargas N (2011) Tribocorrosion mechanisms in sliding contacts. In: Landolt D, Mischler S (eds) *Tribocorrosion of passive metals and coatings*. Woodhead Publishing, Lausanne
  15. von der Ohe CB, Johnsen R, Espallargas N (2010) Modeling the multi-degradation mechanisms of combined tribocorrosion interacting with static and cyclic loaded surfaces of passive metals exposed to seawater. *Wear* 269:607–616
  16. Papageorgiou N, Mischler S (2012) Electrochemical simulation of the current and potential response in sliding tribocorrosion. *Tribol Lett* 48:271–283
  17. Espallargas N, Johnsen R, Torres C (2013) A new experimental technique for quantifying the galvanic coupling effects on stainless steel during tribocorrosion under equilibrium conditions. *Wear* 307:190–197
  18. Vieira AC et al (2012) Mechanical and electrochemical deterioration mechanisms in the tribocorrosion of Al alloys in NaCl and in NaNO<sub>3</sub> solutions. *Corros Sci* 54:26–35
  19. Diomidis N et al (2010) Tribocorrosion of stainless steel in sulfuric acid: Identification of corrosion-wear components and effect of contact area. *Wear* 269:93–103
  20. Favero M, Stadelmann P, Mischler S (2006) Effect of the applied potential of the near surface microstructure of a 316L steel submitted to tribocorrosion in sulfuric acid. *J Phys D Appl Phys* 39:3175–3183
  21. Perret J et al (2010) EBSD, SEM and FIB characterisation of subsurface deformation during tribocorrosion of stainless steel in sulphuric acid. *Wear* 269:383–393
  22. Bazzoni A, Mischler S, Espallargas N (2013) Tribocorrosion of pulsed plasma-nitrided CoCrMo implant alloy. *Tribol Lett* 49:157–167
  23. Wei R et al (2004) High-intensity plasma ion nitriding of orthopedic materials: part I, tribological study. *Surf Coat Technol* 186:305–313
  24. Lanning BR, Wei R (2004) High intensity plasma ion nitriding of orthopedic materials: part II, microstructural analysis. *Surf Coat Technol* 186:314–319
  25. Elik C et al (2008) Effects of plasma nitriding on mechanical and tribological properties of CoCrMo alloy. *Surf Coat Technol* 202:2433–2438
  26. Pichon L et al (2010) CoCrMo alloy treated by floating potential plasma assisted nitriding and plasma based ion implantation: influence of the hydrogen content and of the ion energy on the nitrogen incorporation. *Surf Coat Technol* 204:2913–2918
  27. Ozturk O, Trkan U, Eroglu A (2006) Metal ion release from nitrogen ion implanted CoCrMo orthopedic implant material. *Surf Coat Technol* 200:5687–5697
  28. Zavieh AH, Espallargas N (2016) Effect of 4-point bending and normal load on the tribocorrosion-fatigue (multi-degradation) of stainless steels. *Tribol Int* 99:96–106
  29. Zavieh AH, Espallargas N (2016) The role of surface chemistry and fatigue on tribocorrosion of austenitic stainless steel. *Tribol Int* 103:368–378
  30. Zavieh AH, Espallargas N (2017) The effect of friction modifiers on tribocorrosion and tribocorrosion-fatigue of austenitic stainless steel. *Tribol Int* 111:368–378
  31. McCafferty E (2009) *Thermodynamics of corrosion: pourbaix diagrams. Introduction to corrosion science*. Springer, New York, pp 95–117
  32. Vidal CV, Munoz AI (2011) Electrochemical aspects in biomedical alloy characterization: electrochemical impedance spectroscopy, biomedical engineering, trends in materials science. InTech, London
  33. Galant NJ (2012) Disulfidicity: a scale to characterize the disulfide bond strength via the hydrogenation thermodynamics. *Chem Phys Lett* 539:11–14